



Near-Infrared Electron Acceptors with Fluorinated Regioisomeric Backbone for Highly Efficient Polymer Solar Cells

Fang-Xiao Chen, Jing-Qi Xu, Zhi-Xi Liu, Ming Chen, Ruoxi Xia, Yongchao Yang, Tsz-Ki Lau, Yingzhu Zhang, Xinhui Lu, Hin-Lap Yip, Alex K.-Y. Jen, Hongzheng Chen, and Chang-Zhi Li*

Solar photon-to-electron conversion with polymer solar cells (PSCs) has experienced rapid development in the recent few years. Even so, the exploration of molecules and devices in efficiently converting near-infrared (NIR) photons into electrons remains critical, yet challenging. Herein presented is a family of near-infrared nonfullerene acceptors (NIR NFAs, T1–T4) with fluorinated regioisomeric A–A π –D–A π –A backbones for constructing efficient single-junction and tandem PSCs with photon response up to 1000 nm. It is found that the tuning of the regioisomeric bridge (A π) and fluoro (F)-substituents on a molecular skeleton strongly influences the backbone conformation and conjugation, leading to the optimized optoelectronic and stable stacking of resultant NFAs, which eventually impacts the performance of derived PSCs. In PSCs, the proximal NFAs with varied F-atoms (T1–T3) mostly outperform than that of distal NFA (T4). Notably, single-junction PSC with PTB7-Th:T2 blend can reach 10.87% power conversion efficiency (PCE), after implementing a solvent additive to improve blend morphology. Moreover, efficient tandem PSCs are fabricated through integrating such NIR cells with mediate bandgap nonfullerene-based subcells, to achieve a PCE of 14.64%. The results reveal the structural design of organic semiconductor and device with improved photovoltaic performance.

chemical versatility of organic semiconductors.^[7–13] For instance, the recent development of near-infrared (NIR) organics (bandgap, $E_g < 1.4$ eV) enables PSCs with strong NIR photon responsiveness and visible-range transparency, which are promising for constructing tandem and semitransparent PSCs.^[14–23]

Although considerable efforts have been devoted to developing NIR organic semiconductors, PSCs based on NIR donor and fullerene acceptors usually show PCE lower than 10% and suffer from relatively low external quantum efficiencies (EQE).^[24,25] Encouragingly, the recent development of fused-ring nonfullerene acceptors (NFAs), such as IHIC,^[26] IEICO,^[27] ATT-2,^[28] BT-CIC,^[29,30] DTPC-IC,^[31] and CO δ DFIC,^[32] provides new opportunities, which enables PSCs to utilize NIR photons for achieving high short-circuit current (J_{SC}). Since low-energy NIR photons are inclined to photothermic conversion within organics, it is still challenging to achieve NIR photon-to-electron

conversion with high quantum efficiency and less energy loss in PSCs.^[33] Also, the access of optimal bulk heterojunction (BHJ) blend morphologies, which impacts largely to the overall performance of PSCs, is usually obtained via the trial-and-error

The field of polymer solar cells (PSCs) has continuously advanced over the past few years due to the fast evolution of novel electroactive molecules.^[1–6] One promising virtue for PSCs is their functional tunabilities stemming from the

F.-X. Chen, J.-Q. Xu, Z.-X. Liu, M. Chen, Y. Zhang, Prof. A. K.-Y. Jen, Prof. H. Chen, Prof. C.-Z. Li
State Key Laboratory of Silicon Materials
MOE Key Laboratory of Macromolecular Synthesis and Functionalization
Department of Polymer Science and Engineering
Zhejiang University
Hangzhou 310027, P. R. China
E-mail: czli@zju.edu.cn
J.-Q. Xu, Prof. A. K.-Y. Jen
Department of Materials Science and Engineering
University of Washington
Seattle, WA 98195-2120, USA

R. Xia, Y. Yang, Prof. H.-L. Yip
State Key Laboratory of Luminescent Materials and Devices
School of Materials Science and Engineering
South China University of Technology
381 Wushan Road, Guangzhou 510640, P. R. China
T.-K. Lau, Prof. X. Lu
Department of Physics
The Chinese University of Hong Kong
New Territories, Hong Kong 999077, P. R. China
Prof. A. K.-Y. Jen
Department of Materials Science & Engineering
City University of Hong Kong
Kowloon, Hong Kong 999077, P. R. China

The ORCID identification number(s) for the author(s) of this article can be found under <https://doi.org/10.1002/adma.201803769>.

DOI: 10.1002/adma.201803769

processing,^[34] which is somehow impractical to scale up fabrication. So far, few as-cast PSCs yielded PCEs > 8%, considering both fullerene-based and NFA-based devices,^[28,35,36] hence there is a strong need to explore the structural design of NIR photoactive molecules that allow improvement of BHJ characteristics, such as charge mobilities and morphological domains, to eventually optimize PSC device operation, especially in the process of low-energy NIR photon-to-electron conversion.

Additionally, single organic BHJ layer with an optimal thickness of 100 nm typically results in incomplete photon absorption and encounters noticeable energy loss.^[37] High-energy photons beyond the optical band gap of organics face energy loss through the relaxation of excitons into the lowest excited state. And low energy photons below the optical band gaps are just unabsorbed.

In this regard, tandem device connects subcells with complementary absorption in series, which facilitates the simultaneous utilization of high- and low-energy photons, thus displaying higher efficiency ceiling than single-junction PSC.^[16,19,22,38,39] Nevertheless, significant challenges remain to construct efficient tandem devices, including the lack of efficient NIR materials, the sophisticated fabrication, and optical balance between subcells.

Herein, four new NIR NFAs with fluorinated regioisomeric A-A π -D-A π -A backbone, including IFIC-i-2F (T1), IFIC-i-4F (T2), IFIC-i-6F (T3), and IFIC-o-4F (T4) are developed for constructing efficient single-junction and tandem PSCs. IFIC represents new NFA backbone, in which indacenodithiophene (IDT, D) electron-donating core connects to electron-withdrawing 1,1-dicyanomethylene-3-indanone (IC, A), through an unsymmetrical fluorothiopheno[3,4-b]thiophene (FTT, A π) bridge in a regioisomeric fashion (proximal vs distal) (Figure 1). The proximal (or distal) isomer refers to fluoro (F)-atom on FTT pointing to (or away) IDT in IFIC structure, respectively. This arrangement modulates the backbone rigidity and planarity as well as internal charge transfer of resultant IFICs, hence influences the optoelectronic and robust stacking properties. These four IFICs exhibit broad absorption (with E_g down to 1.27 eV), and fine-tuned energy levels. Interestingly, though with similar molecular formula, a significant increase of PSC performance can be observed from distal NFA, 7% (T4) to proximal NFAs with varied F-atoms (T1-T3), up to 10.10% (T2), through the simple solution-cast with PTB7-Th polymer.

The reason ascribed is that the close junction of F-atom in FTT to IDT in proximal NFA promotes intramolecular F-S/F-H interaction. And thus the proximal NFA has a more rigid and planar molecular skeleton over distal NFA, resulting in strong stacking and high electron mobilities. Besides,

proximal NFA possesses the upshifted energetics over distal NFA due to avoiding of further conjugation with electron-withdrawing ester and the double bond of FTT with terminal IC. This simultaneously helps mitigating the energy loss and enhancing EQE of PSCs with proximal NFA over those with distal NFA. The optimal performance for T2:PTB7-Th-based PSCs can be further improved by proceeding with 1% 1-chloronaphthalene (CN) as the solvent additive, showing impressive PCE of 10.87% with high J_{SC} of 24.85 mA cm⁻², V_{OC} of 0.65 V, and FF of 0.67. Interestingly, efficient tandem solar cells can be constructed by integrating NIR-absorbed IFIC-4F (T2): PTB7-Th subcell with mediate bandgap ITIC:PBDB-T subcell.^[7,40] Together with careful optical simulation and device engineering, high PCE of 14.64% is achieved for the absorption

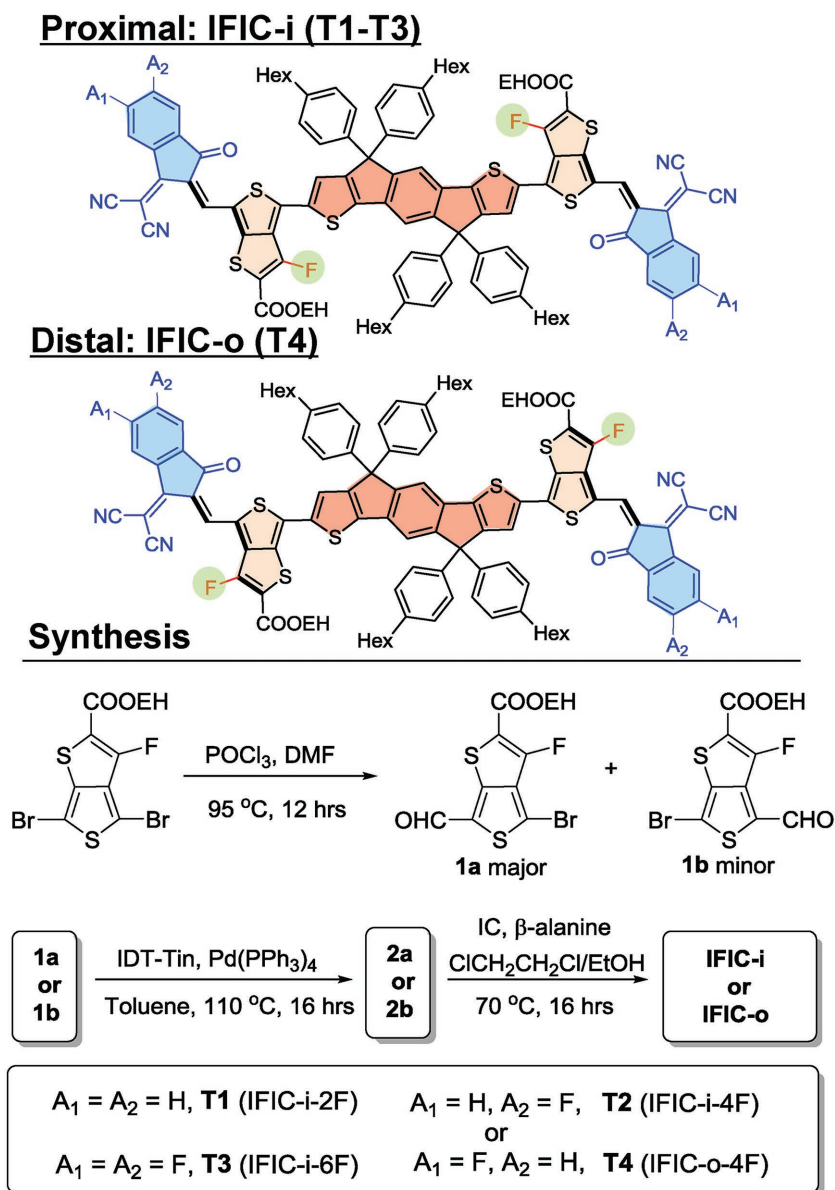


Figure 1. Chemical structures and the synthetic route for T1 (IFIC-i-2F), T2 (IFIC-i-4F), T3 (IFIC-i-6F), and T4 (IFIC-o-4F).

range up to ≈ 1000 nm, which is one new example among the best performing tandem PSCs to date. This study reveals new insights on the structural design of NIR organics and devices with improved photovoltaic performance.

Figure 1 shows the chemical structures of four NIR NFAs. The synthesis is accomplished in three steps from the commercially available dibromo-2-Ethylhexyl-3-fluorothieno[3,4-*b*]thiophene-2-carboxylate (Br-FTT), with details described in the Supporting Information. Briefly, formylation of Br-FTT via Vilsmeier–Haack reaction yields two regioisomers, with 4-aldehyde compound **1a** as the major compound compared to 6-aldehyde **1b**, due to the regio- and chemopreference of unsymmetrical FTT.^[41] Both can be separated via a Silica Gel column. Then, compound **2a** (or **2b**) is obtained through Stille cross-coupling of IDT-Tin with **1a** (or **1b**), respectively. Finally, NIR NFAs, T1–T4 are obtained by Knoevenagel reaction of **2a** (or **2b**) and IC with different F-substituents. They are soluble in common organic solvents such as chloroform, chlorobenzene at room temperature. The chemical structure of each new compound is fully characterized by ¹H NMR, ¹³C NMR, and Mass spectra (Supporting Information).

New NFAs exhibit broad absorption extended into NIR region and slightly varied energy levels. Their optoelectronic properties in film and chloroform (CHCl₃) solution are summarized in Table 1. The film absorption onsets of T1, T2, T3, and T4 are 928, 968, 976, and 976 nm, corresponding to the E_g of 1.34, 1.30, 1.27, and 1.27 eV, respectively. Interestingly, the maximum absorption of T2, T3, and T4 exhibits over ≈ 50 nm redshift from solution to film, larger than those of T1 (≈ 45 nm redshift) (Table 1, Figure 2a and Figure S1, Supporting Information). Also, the Stokes shift ($\Delta\lambda_{\text{shift}}$) between absorption maximum ($\lambda_{\text{max}}(\text{F})$) and film emission maximum ($\lambda_{\text{emission}}$) is also varied for these four film samples, 164 nm (T1), 151 nm (T2), 140 nm (T3), and 158 nm (T4). These observations indicate that the introduction of F-atoms into IC terminals intensifies solid state stacking of NFAs, which can be ascribed to the presence of intra- and intermolecularly noncovalent F–S and F–H bonding.^[42–45]

Theoretical calculations (Supporting Information) suggest that the close junction of F-atom in FTT to IDT in proximal NFA not only hinders the conformation rotation of molecule (enlarging single bond ratio barrier between IDT and bridge from distal to proximal NFAs), but also planarizes the backbone (the dihedral angle between IC and bridge, 0.22° vs 5.84° for proximal and distal NFAs, Figure 2b). These, in turn, result in an optimal orbital hybrid of A–A _{π} –D–A _{π} –A backbone, thus facilitating the intracharge transfer of proximal NFAs (Figures S2 and S3, Supporting Information). To distinct the effect of isomeric molecular geometry (T2 and T4) on their stacking behaviours,

grazing-incidence wide-angle X-ray scattering (GIWAXS) is employed (Figure 2c,d and Figure S6, Supporting Information), indicating both molecules take predominantly face-on orientation relative to the electrode substrates. In details, T2 (IFIC-i-4F) and T4 (IFIC-o-4F) samples present sharp peaks (100) at $\approx 0.310 \text{ \AA}^{-1}$, corresponding to a lamellar d-spacing of 20.3 \AA , respectively. A clear reflection (010) peak could be observed at 1.80 \AA^{-1} for T2, which corresponds to the d-spacing for π – π stacking of 3.49 \AA . However, T4 shows quite weak and broad (010) peak at 1.77 \AA^{-1} , corresponding to a d-spacing of 3.55 \AA . Also, proximal T2 shows significantly stronger peak intensity, indicating better self-organization behavior and crystallinity over distal T4, which may stem from the planar and rigid backbone of proximal NFAs.

In addition, the lowest unoccupied molecular orbitals (LUMOs, -3.91 eV of T1, -3.96 eV of T2, -4.00 eV of T3, and -4.01 eV of T4) of NFAs are downshifted with the increase of F-contents on backbone, clearly indicated by cyclic voltammetry (CV) measurements (Figure S4, Supporting Information). It is also worthy to note that the bridge isomer affects the energetics of NFAs, showing the proximal T2 (-3.96 eV) has an upshifted LUMO than that of distal T4 (-4.01 eV). It can be ascribed to the proximal bridge isomer avoiding further conjugating electron-withdrawing ester and double bond on FTT with terminal IC unit (Figure 2b and Figure S5, Supporting Information).

With the above information, their photovoltaic properties are investigated with an inverted architecture of indium tin oxide (ITO)/ZnO/PTB7-Th:NFAs/MoO₃/Ag. The current density–voltage (J – V) curves are displayed in Figure 3a, and the device parameters are summarized in Table 2. The optimized PTB7-Th:NFAs weight ratio is 1:1.8. Fluorination of IC slightly decreases V_{OC} of PSCs from 0.72 to 0.61 V (T1–T3), which is consistent with the trend of lowering their LUMO levels. Noticeably, the devices based on T1 show a J_{SC} value of 20.95 mA cm^{-2} , while T2 and T3 enhance J_{SC} to $\approx 22 \text{ mA cm}^{-2}$, which is attributed to their red-shifted absorption as well as the enhanced EQEs at NIR region (Figure 3b). Also, fill factor (FF) increases from 0.65 (T1) to 0.70 (T3), as the number of F-atoms increases. As a result, the averaged PCEs based on as-cast PTB7-Th: T1, PTB7-Th: T2, and PTB7-Th: T3 are 9.67%, 10.01%, and 9.23%, respectively. And, PTB7-Th: T2 blends show the best PCE of 10.10% with a V_{OC} of 0.67 V, a J_{SC} of 22.65 mA cm^{-2} , and an FF of 0.67. More interestingly, the effects of bridge isomers on their photovoltaic properties are studied, showing that proximal T2 blends (10.10% PCE) possess significantly higher PCEs than T4 (7% PCE), because of the simultaneous increments of all parameters in the T2 blend. The blend morphology of films is investigated by transmission electron microscopy (TEM) (Figure S7, Supporting Information), showing both PTB7-Th and NFAs possess clear contrast on nanoscale phase separation.

To better understand the reason of performance variation on structural changes, the hole and electron mobilities of four blends are measured using the space-charge-limited-current (SCLC) method (Table 2). Interestingly, the observed electron mobilities are highly dependent on the isomeric bridge and

Table 1. Optoelectronic properties of NFAs, T1–T4.

	$\lambda_{\text{max}}(\text{S})$ [nm]	$\lambda_{\text{max}}(\text{F})$ [nm]	$\lambda_{\text{onset}}(\text{F})$ [nm]	$\lambda_{\text{emission}}$ [nm]	$\Delta\lambda_{\text{Shift}}$ [nm]	E_g [eV]	HOMO [eV]	LUMO [eV]
T1	776	824	928	988	164	1.34	–5.42	–3.91
T2	789	845	968	996	151	1.30	–5.34	–3.96
T3	790	850	976	990	140	1.27	–5.31	–4.00
T4	794	848	976	1006	158	1.27	–5.36	–4.01

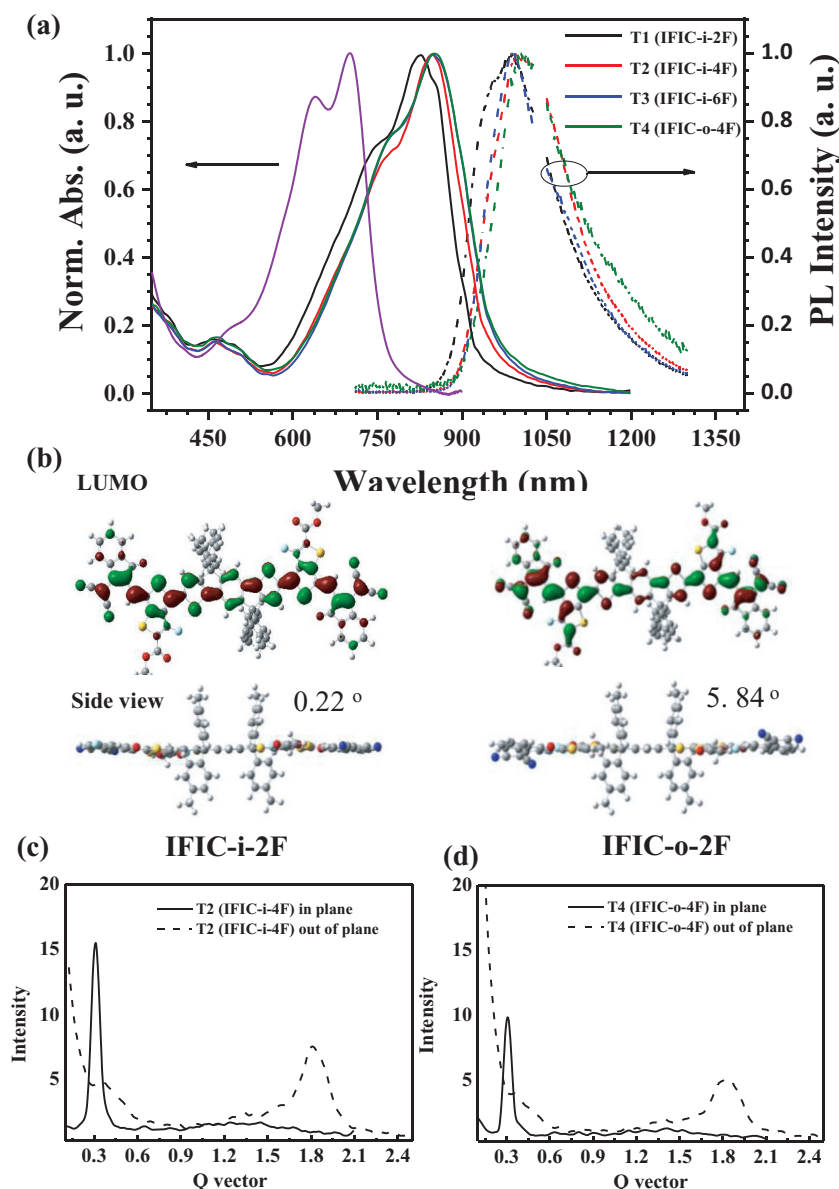


Figure 2. a) The normalized UV-vis absorption of T1–T4 and PTB7-Th films and PL emission spectra of T1–T4 films; b) the optimized molecular conformation and LUMO obtained from DFT calculations (Supporting Information). The dihedral angles between terminal IC and FTT are 0.22° (proximal IFIC-i-2F) and 5.84° (distal IFIC-o-2F), respectively. c,d) In-plane and out-of-plane GIWAXS diffraction profiles of T2 (c) and T4 (d) films.

F-content of NFAs. Notably, the proximal T1–T3 blends (2.26×10^{-4} , 4.68×10^{-4} , and $7.88 \times 10^{-4} \text{ cm}^2 \text{ V}^{-1} \text{ s}^{-1}$, respectively) show one order of magnitude higher electron mobility than the distal T4 ($0.34 \times 10^{-4} \text{ cm}^2 \text{ V}^{-1} \text{ s}^{-1}$). It is consistent with the GIWAXS results discussed above that the relatively shorter π - π stacking distance and improved crystallinity for proximal isomer (T2) film are favorable for electron transport. As their hole mobilities are similar (4.54 – $5.36 \times 10^{-4} \text{ cm}^2 \text{ V}^{-1} \text{ s}^{-1}$), T1–T3 blends exhibit more balanced charge transport several times higher than T4 blend. Another observed trend is the increase of proximal NFA electron mobilities with introduction of more F-atoms. These may be ascribed to the noncovalent F–S, and F–H interaction

that intensifies solid stacking of NFAs. As a result, with a rigid and planar backbone, proximal NFA-based blends exhibit improved electron mobilities and balanced charge transport than the distal NFA blends, which can be responsible for their higher J_{SC} and EQE in PSCs.

Furthermore, PTB7-Th:T2 active layer was optimized by utilizing solvent additives. It can be identified that the J_{SC} value improved from 22.65 to 24.85 mA cm^{-2} , when the film was processed with 1% v/v CN additive, leading to an improved PCE of 10.87% (Figure 4a). EQE curves (Figure 4b) for the optimized device exhibit a high photon response from 450 to 950 nm, up to 0.81, indicating the improved photon harvesting and charge collection in CN-additive-processed blends. The integrated J_{SC} values from EQE spectra for PTB7-Th: T1–T4 are 19.97, 22.01, 20.05, and 17.74 mA cm^{-2} , and for the PSC with highest J_{SC} from PTB7-Th: T2 (with CN) is 24.01 mA cm^{-2} , which agrees well with the experimental J_{SC} value of 24.85 mA cm^{-2} . The J_{SC} versus light intensity (P) curves were measured to study charge recombination behavior (Figure 4c). The relationship between J_{SC} and P can be described as $J_{\text{SC}} \propto P^\alpha$. If all the charges are swept out and collected by the electrode, then bimolecular recombination is negligible, α should be close to 1. It is shown that the device with CN-additive-based blend ($\alpha = 1.00$) has slightly higher α than that with the as-cast blend ($\alpha = 0.987$), suggesting that bimolecular recombination is suppressed for the CN-additive-processed device.

The effect of solvent additive on the blend morphologies is studied by the topography photoinduced force microscopy (PiFM).^[46] As shown in Figure 4d, PTB7-Th and T2 have characteristic Fourier transform infrared (FT-IR) absorption peaks, associated with their chemical structure. By imaging at 1315 cm^{-1} for T2 and 1720 cm^{-1} for PTB7-Th with PiFM, spatially mapped patterns of PTB7-Th and T2 in their top surface of blend films are clearly visible. As depicted in Figure 4e,f, relatively intimate mixing between the two components is observed for the as-cast PTB7-Th:T2 films. While proper phase separation in PTB7-Th:T2 blend is gauged from PiFM measurements that exhibit an average domain size ≈ 20 nm at top surface of blend film when processed with 1% v/v CN additive. If similar phase separation presents in bulk, it would not only facilitate exciton dissociation, but also enables a continuous network for carrier transport retarding spatial charge recombination in blends, leading to an increase in J_{SC} , FF, as well as device efficiency.

Based on the single-junction PSCs achieved above, we further constructed inverted tandem PSCs with the structure of

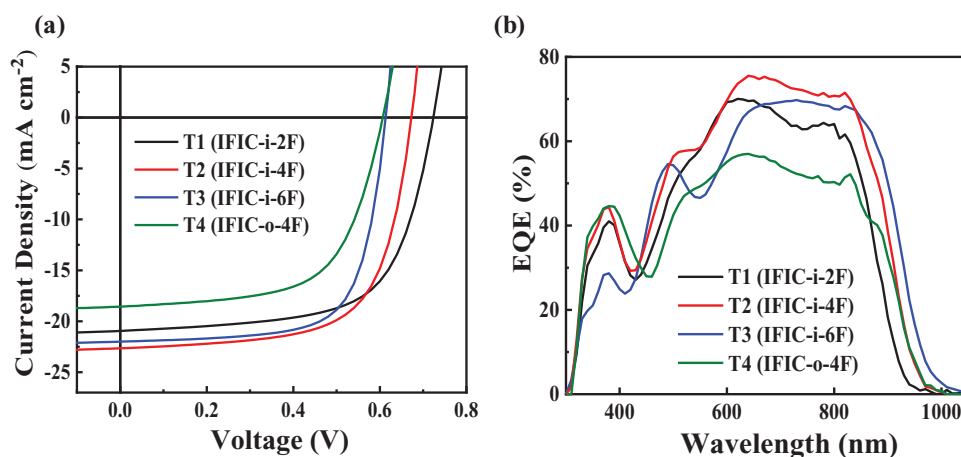


Figure 3. a) The J - V characteristics and b) EQE spectrum of the resultant PSCs for the inverted single junction PSC with NIR BHJs (PTB7-Th:T1-T4).

ITO/ZnO/PBDB-T:ITIC/MoO₃/Ag/ZnO-NP/PFN-Br/PTB7-Th:IFIC-i-4F(T2)/MoO₃/Ag (Figure 5a). A functional interconnecting layer (ICL) is fabricated in the structure of MoO₃/ultrathin Ag/zinc oxide nanoparticle (ZnO-NP)/poly[(9,9-bis(3-(*N,N*-dimethylammonium)-propyl)-2,7-fluorene)-*alt*-2,7-(9,9-dioctyl-fluorene)] Bromide (PFN-Br), which can be clearly visualized from the cross-sectional scanning electron microscopy (SEM) image of tandem PSCs (Figure 5b). The schematic energy diagram of each layer is shown in Figure 5c, indicating the proper energy level alignment of each component in the device. We have previously demonstrated the first example of tandem devices containing all-solution-processed nonfullerene BHJs in both front and rear cells,^[19] in which ICL not only promotes the quasi-ohmic contact of subcells for efficient charge recombination, but also adjusts the optical field distribution of each cell. Since the overall J_{SC} in series tandem OSCs is limited by the lowest current density value of subcell, to balance photon distribution of two subcells, optical modelling based on the transfer matrix method was carried out to probe for the optimal thicknesses of the subcells and ICL. The refractive index (n) and extinction coefficient (k) of the different layers used in the tandem devices were measured by a spectroscopic ellipsometer. The simulated results indicate that one of optimum J_{SC} values (Figure S8, Supporting Information) and photon absorption distribution (Figure S9, Supporting Information) within the tandem device can be achieved with comfortable thickness of front PBDB-T:ITIC cell (100 nm) and rear PTB7-Th:T2 cell (120 nm) with an ultrathin silver layer in the ICL.

For device fabrication, we varied the thickness of the ultrathin silver layer in the ICL as well as the front and rear

cells to tune the optical field distribution and ensure efficient charge recombination between two subcells. J - V curves of tandem devices with different silver thickness (from 0 to 4, 7, and 10 nm) in the ICL and corresponding device performance parameters are summarized in Figure S10 and Table S1 in the Supporting Information. After tuning the thicknesses for front and rear cells, the highest performance among these conditions is achieved with a PCE of 14.64% (V_{OC} of 1.56 V, J_{SC} of 13.22 mA cm⁻², and FF of 0.71) under 7 nm silver layer in the ICL (Figure 5d and Table S2, Supporting Information). Note that the incorporation of PFN-Br layer atop ZnO-NP allows improving device parameters slightly, compared to devices without PFN-Br (Figure S11, Supporting Information), which may be ascribed to the adjustment of the energetics and surface passivation of ZnO-NP on introduction of PFN-Br. The EQE value of the front cell reaches ~60% in 300–800 nm with integrated J_{SC} of 12.45 mA cm⁻². The rear cell showed a broad EQE spectrum with a low response in the short wavelength region (300–700 nm) and high response over 70% at the long wavelength region (700–1000 nm), which corresponds to an integrated J_{SC} of 12.57 mA cm⁻² (Figure S12, Supporting Information). The efficiencies of tandem device with and without aperture are also later evaluated from the individual fabrication of devices, showing the relative performance deviation ~ 5% (i.e., PCE of 14.05% without aperture and 13.29% with aperture, Figure S13, Supporting Information). The achieved V_{OC} nearly equals to the summed value (1.57 V) of two subcells, indicating ICL worked well in tandem devices. Further increasing the thickness of the Ag layer to

Table 2. Device performances of the PSCs based on PTB7-Th:T1–T4 blends.

BHJ ^{a)}	Treatment	V_{oc} [V]	J_{sc} [mA cm ⁻²]	FF	PCE ^{b)} [%]	μ_e [$\times 10^{-4}$ cm ² V ⁻¹ s ⁻¹]	μ_h [$\times 10^{-4}$ cm ² V ⁻¹ s ⁻¹]	μ_e/μ_h
PTB7-Th:T1	As cast	0.72	20.95	0.65	9.82 (9.67 ± 0.13)	2.26	5.09	0.44
PTB7-Th:T2	As cast	0.67	22.65	0.66	10.10 (10.01 ± 0.08)	4.68	5.36	0.87
PTB7-Th:T3	As cast	0.61	22.00	0.70	9.43 (9.23 ± 0.20)	7.88	4.54	1.73
PTB7-Th:T4	As cast	0.61	18.57	0.62	7.01 (6.86 ± 0.21)	0.34	5.98	0.06
PTB7-Th:T2 ^{c)}	1% CN	0.65	24.85	0.67	10.87 (10.65 ± 0.20)	5.10	5.40	0.94

^{a)}All blends are donor:acceptor weight ratio of 1:1.8; ^{b)}The averaged PCEs based on 20 devices are shown in parentheses.

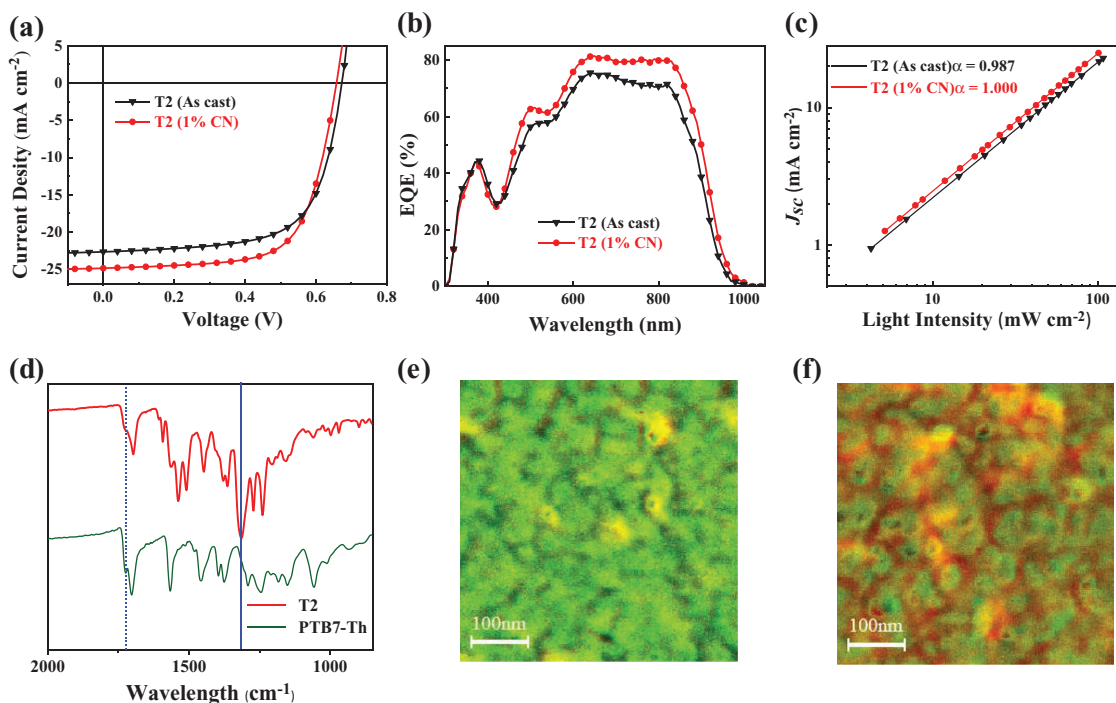


Figure 4. a) The J - V characteristics, b) EQE spectrum, c) J_{SC} -light intensity dependence measurements of the PSCs based on PTB7-Th:T2 with and without CN additive, and d) FT-IR spectra of T2 and PTB7-Th. e, f) PiFM images of the as-cast (e) and with 1% CN (f) PTB7-Th:T2 blend films examined at 1720 and 1315 cm^{-1} corresponding to the absorption bands for PTB7-Th and T2, respectively. The spectral response for PTB7-Th component is marked with green and with red for T2.

10–15 nm, tandem devices exhibited decreased V_{OC} (≈ 1.52 V) and lowered J_{SC} values, because of the mismatched optical field distribution and insufficient charge recombination between subcells.

In summary, new NIR NFAs with E_g as low as 1.27 eV are developed through tailoring the A-A π -D-A π -A molecular backbones, in which an unsymmetrical bridge is employed to the conjugate electron-donating core with electron-withdrawing

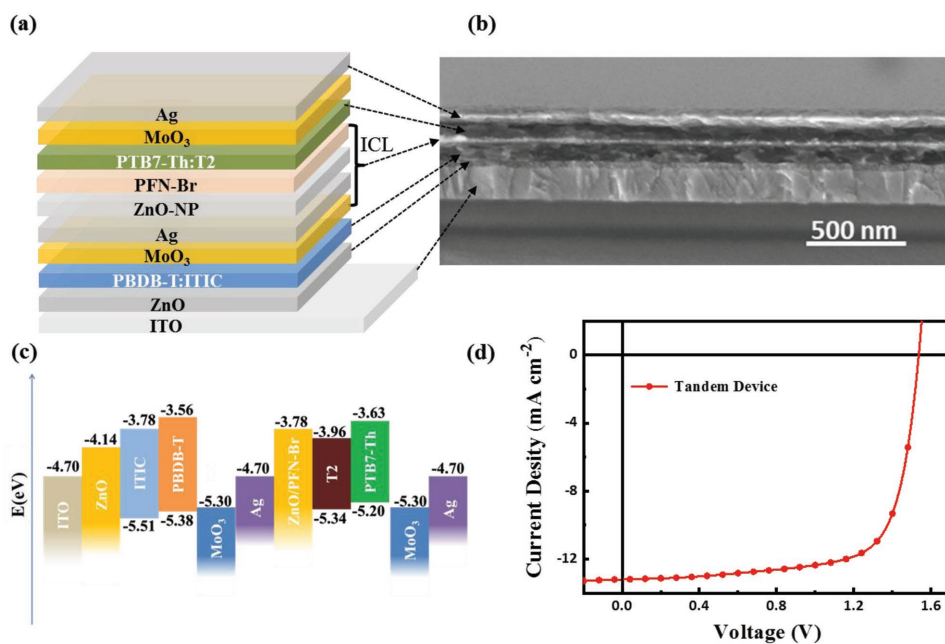


Figure 5. a) Schematic architecture and b) cross-sectional SEM image for tandem PSCs. c) Energy levels of each layer and d) optimal J - V curves of the tandem device under the illumination of AM 1.5G (100 mW cm^{-2}).

terminals, in a region-isomeric fashion. Such arrangement allows useful modulation of the backbone conformation and orbital hybridization of resultant NFAs, hence influencing their optoelectronic and solid stacking properties. Although with identical molecular formula, the derived PSCs with solution-cast blends allow significantly improved PCEs from 7% (distal NFA, T4) to 10.10% (proximal NFAs, T2), due to the mitigated energy loss and enhanced quantum efficiency in proximal NFA-based PSCs over distal NFA. The performance for T2:PTB7-Th-based PSCs can be further optimized by proceeding with 1% CN additive, showing an impressive PCE of 10.87% with EQE up to 0.81. More interestingly, efficient tandem PSCs are also constructed by integrating this NIR cell with mediate bandgap cell, together with optical simulation and device engineering. High PCE of 14.64% is achieved for a tandem device with the absorption up to ≈ 1000 nm, which is one new example among the best-performing tandem PSCs to date. Our studies revealed that the tailoring of the regio-isomeric backbone of NIR NFAs could directly impact their BHJ blend characteristics, eventually optimizing solar cell operation, especially in the process of low-energy NIR photon-to-electron conversion. These results reveal new insights into the structural design of NIR organic semiconductors and their related devices, to further improve the performance of PSCs.

Experimental Section

Device Fabrication and Characterization: PSCs fabricated on glass substrates commercially precoated with a layer of indium tin oxide (ITO) with the inverted structure of ITO/ZnO/PTB7-Th:Acceptors/MoO₃/Ag for single-junction PSC, and with the structure of ITO/ZnO/PBDD-T:ITIC/MoO₃/Ag/ZnO-NP/PFN-Br/PTB7-Th:IFIC-4F(T2)/MoO₃/Ag for tandem PSCs. Before fabrication, the substrates were cleaned using detergent, deionized water, acetone, and isopropanol consecutively for every 15 min, and then treated in an ultraviolet ozone generator for 5 min. The sol-gel ZnO was fabricated from zinc dihydrate acetate solution in 2-methoxyethanol and 2-aminoethanol.

Single-Junction Cell Fabrication: A thin layer of sol-gel ZnO was fabricated by spin coating of zinc dihydrate acetate solution onto precleaned ITO-coated glass substrates at 3500 rpm for 60 s and then annealed at 170 °C for 20 min. Then the substrates were transferred into a glovebox; the active layer was spin coated from 20 mg mL⁻¹ chlorobenzene solution of PTB7-Th: IFICs (1:1.8 wt%) with or without CN additive at 2000 rpm for 60 s. Finally, a layer of MoO₃ (4 nm) and the Ag (100 nm) electrode were deposited by thermal evaporation to complete the device with an active area of 6 mm².

Tandem Cell Fabrication: The active layer for the front cell was first spin-coated atop ZnO/ITO substrates with 20 mg mL⁻¹ chlorobenzene (with 0.5 vol% DIO) solution of PBDD-T: ITIC (1:1 wt%) at 2500 rpm for 60 s, and annealed at 100 °C for 10 min. Then, MoO₃ (8 nm) and ultrathin Ag with different thickness were deposited via thermal evaporation. The deposition of the ultrathin Ag layer was defined by a mask with good alignment to the patterned ITO strip. Atop ultrathin Ag layer, ZnO-NP and PFN-Br in methanol were subsequently spin-coated to complete ICL fabrication. (Note that the ICL layer was later divided into separated pieces with a scalpel according to the top silver electrodes). Afterward, the active layer for the rear cell was spin-coated from 23 mg mL⁻¹ chlorobenzene solution of PTB7-Th: IFIC-4F (1:1.8 wt%) at 2500 rpm for 60 s. The tandem device was completed by evaporating 4 nm MoO₃ and 100 nm Ag. The active area of tandem PSCs is 6 mm² (without aperture) and 3.75 mm² (with aperture) (Figure S13, Supporting Information).

The *J*-*V* curves of OSCs were measured with Keithley 2400, under AM 1.5G illumination at 100 mW cm⁻² irradiation using a Enli SS-F5-3A solar simulator, and the light intensity was calibrated with a standard Si solar cell with KG5 filter (made by Enli Technology Co., Ltd., Taiwan, and calibrated report can be traced to NREL). The EQE spectrum was measured using a QE-R Solar Cell Spectral Response Measurement System (Enli Technology Co., Ltd., Taiwan). For EQE of subcells in tandem devices, a third electrode was adopted for the measurement of the front and back cells separately using following protocol: after evaporation of the ultrathin silver layer in the ICL, an indium stripe on the silver layer in the ICL was pasted at one side before the fabrication of the back cell. Later, the individual subcell in an integrated tandem device can be separately measured through the selective connection of indium electrode to either top electrode (for rear cell) or ITO (for front cell).

Supporting Information

Supporting Information is available from the Wiley Online Library or from the author.

Acknowledgements

F.-X.C., J.-Q. X., and Z.-X.L. contributed equally to this work. This research was funded by National Natural Science Foundation of China (Nos. 21722404, 21674093, 21734008, and 51473142), 973 program (No. 2014CB643503), the Office of Naval Research (N00014-17-1-2201), International Science and Technology Cooperation Program of China (ISTCP) (Grant No. 2016YFE0102900), the Ministry of Science and Technology (2017YF0206600), and Zhejiang Province Science and Technology Plan (No. 2018C01047). C.-Z.L. thanks the support by Zhejiang Natural Science Fund for Distinguished Young Scholars (LR17E030001), the Young 1000 Talents Global Recruitment Program of China, and 100 Talents Program of Zhejiang University. X.L. thanks Research Grant Council of Hong Kong (Theme-based Research Scheme No. T23-407/13-N).

Conflict of Interest

The authors declare no conflict of interest.

Keywords

near-infrared absorption, nonfullerene acceptors, polymer solar cells, tandem devices

Received: June 14, 2018
Revised: September 30, 2018
Published online:

- [1] Y.-J. Cheng, S.-H. Yang, C.-S. Hsu, *Chem. Rev.* **2009**, *109*, 5868.
- [2] H. Yao, L. Ye, H. Zhang, S. Li, S. Zhang, J. Hou, *Chem. Rev.* **2016**, *116*, 7397.
- [3] Y. Lin, X. Zhan, *Acc. Chem. Res.* **2016**, *49*, 175.
- [4] C. B. Nielsen, S. Holliday, H.-Y. Chen, S. J. Cryer, I. McCulloch, *Acc. Chem. Res.* **2015**, *48*, 2803.
- [5] C.-C. Chueh, C.-Z. Li, A. K. Y. Jen, *Energy Environ. Sci.* **2015**, *8*, 1160.
- [6] S. Li, W. Liu, C.-Z. Li, M. Shi, H. Chen, *Small* **2017**, *13*, 1701120.

- [7] Y. Lin, J. Wang, Z. G. Zhang, H. Bai, Y. Li, D. Zhu, X. Zhan, *Adv. Mater.* **2015**, *27*, 1170.
- [8] Y. Liu, Z. Zhang, S. Feng, M. Li, L. Wu, R. Hou, X. Xu, X. Chen, Z. Bo, *J. Am. Chem. Soc.* **2017**, *139*, 3356.
- [9] S. Holliday, R. S. Ashraf, A. Wadsworth, D. Baran, S. A. Yousaf, C. B. Nielsen, C.-H. Tan, S. D. Dimitrov, Z. Shang, N. Gasparini, M. Alamoudi, F. Laquai, C. J. Brabec, A. Salleo, J. R. Durrant, I. McCulloch, *Nat. Commun.* **2016**, *7*, 11585.
- [10] J. Zhao, Y. Li, G. Yang, K. Jiang, H. Lin, H. Ade, W. Ma, H. Yan, *Nat. Energy* **2016**, *1*, 15027.
- [11] X. Xu, T. Yu, Z. Bi, W. Ma, Y. Li, Q. Peng, *Adv. Mater.* **2018**, *30*, 1703973.
- [12] B. Fan, K. Zhang, X. F. Jiang, L. Ying, F. Huang, Y. Cao, *Adv. Mater.* **2017**, *29*, 1606396.
- [13] C.-Z. Li, H.-L. Yip, A. K. Y. Jen, *J. Mater. Chem.* **2012**, *22*, 4161.
- [14] L. X. Meng, Y. M. Zhang, X. J. Wan, C. X. Li, X. Zhang, Y. B. Wang, X. Ke, Z. Xiao, L. M. Ding, R. X. Xia, H. L. Yip, Y. Cao, Y. S. Chen, *Science* **2018**, *361*, 1094.
- [15] Y. Cui, H. Yao, B. Gao, Y. Qin, S. Zhang, B. Yang, C. He, B. Xu, J. Hou, *J. Am. Chem. Soc.* **2017**, *139*, 7302.
- [16] L. Dou, J. You, J. Yang, C.-C. Chen, Y. He, S. Murase, T. Moriarty, K. Emery, G. Li, Y. Yang, *Nat. Photonics* **2012**, *6*, 180.
- [17] L. Zuo, J. Yu, X. Shi, F. Lin, W. Tang, A. K. Y. Jen, *Adv. Mater.* **2017**, *29*, 1702547.
- [18] S. Song, K. Kranthiraja, J. Heo, T. Kim, B. Walker, S.-H. Jin, J. Y. Kim, *Adv. Energy Mater.* **2017**, *7*, 1700782.
- [19] W. Liu, S. Li, J. Huang, S. Yang, J. Chen, L. Zuo, M. Shi, X. Zhan, C. Z. Li, H. Chen, *Adv. Mater.* **2016**, *28*, 9870.
- [20] Y. Zhang, B. Kan, Y. Sun, Y. Wang, R. Xia, X. Ke, Y. Q. Yi, C. Li, H. L. Yip, X. Wan, *Adv. Mater.* **2018**, *30*, 1707508.
- [21] L. Dou, Y. Liu, Z. Hong, G. Li, Y. Yang, *Chem. Rev.* **2015**, *115*, 12633.
- [22] J. Y. Kim, K. Lee, N. E. Coates, D. Moses, T.-Q. Nguyen, M. Dante, A. J. Heeger, *Science* **2007**, *317*, 222.
- [23] Y. Cui, H. F. Yao, C. Y. Yang, S. Q. Zhang, J. H. Hou, *Acta Polym. Sin.* **2018**, *2*, 223.
- [24] C.-C. Chen, L. Dou, J. Gao, W.-H. Chang, G. Li, Y. Yang, *Energy Environ. Sci.* **2013**, *6*, 2714.
- [25] Q. Tai, F. Yan, *Adv. Mater.* **2017**, *29*, 1700192.
- [26] W. Wang, C. Yan, T.-K. Lau, J. Wang, K. Liu, Y. Fan, X. Lu, X. Zhan, *Adv. Mater.* **2017**, *29*, 1701308.
- [27] H. Yao, Y. Chen, Y. Qin, R. Yu, Y. Cui, B. Yang, S. Li, K. Zhang, J. Hou, *Adv. Mater.* **2016**, *28*, 8283.
- [28] F. Liu, Z. Zhou, C. Zhang, J. Zhang, Q. Hu, T. Vergote, F. Liu, T. P. Russell, X. Zhu, *Adv. Mater.* **2017**, *29*, 1606574.
- [29] Y. Li, J.-D. Lin, X. Che, Y. Qu, F. Liu, L.-S. Liao, S. R. Forrest, *J. Am. Chem. Soc.* **2017**, *139*, 17114.
- [30] Y. Li, L. Zhong, B. Gautam, H.-J. Bin, J.-D. Lin, F.-P. Wu, Z. Zhang, Z.-Q. Jiang, Z.-G. Zhang, K. Gundogdu, Y. Li, L.-S. Liao, *Energy Environ. Sci.* **2017**, *10*, 1610.
- [31] Z. Yao, X. Liao, K. Gao, F. Lin, X. Xu, X. Shi, L. Zuo, F. Liu, Y. Chen, A. K. Y. Jen, *J. Am. Chem. Soc.* **2018**, *140*, 2054.
- [32] Z. Xiao, X. Jia, L. Ding, *Sci. Bull.* **2017**, *62*, 1562.
- [33] J. Hou, O. Inganäs, R. H. Friend, F. Gao, *Nat. Mater.* **2018**, *17*, 119.
- [34] S. Kwon, H. Kang, J.-H. Lee, J. Lee, S. Hong, H. Kim, K. Lee, *Adv. Energy Mater.* **2017**, *7*, 1601496.
- [35] Y. Lin, Q. He, F. Zhao, L. Huo, J. Mai, X. Lu, C. J. Su, T. Li, J. Wang, J. Zhu, Y. Sun, C. Wang, X. Zhan, *J. Am. Chem. Soc.* **2016**, *138*, 2973.
- [36] D. Meng, D. Sun, C. Zhong, T. Liu, B. Fan, L. Huo, Y. Li, W. Jiang, H. Choi, T. Kim, J. Y. Kim, Y. Sun, Z. Wang, A. J. Heeger, *J. Am. Chem. Soc.* **2016**, *138*, 375.
- [37] H. Jiang, W. Hanyu, Y. Kangrong, Z. Xiaohua, C. Hongzheng, L. Changzhi, Y. Junsheng, *Adv. Mater.* **2017**, *29*, 1606729.
- [38] M. Li, K. Gao, X. Wan, Q. Zhang, B. Kan, R. Xia, F. Liu, X. Yang, H. Feng, W. Ni, Y. Wang, J. Peng, H. Zhang, Z. Liang, H.-L. Yip, X. Peng, Y. Cao, Y. Chen, *Nat. Photonics* **2017**, *11*, 85.
- [39] X. Che, Y. Li, Y. Qu, S. R. Forrest, *Nat. Energy* **2018**, *3*, 422.
- [40] Z. Wenchao, Q. Deping, Z. Shaoqing, L. Sunsun, I. Olle, G. Feng, H. Jianhui, *Adv. Mater.* **2016**, *28*, 4734.
- [41] H. Zhong, C. Z. Li, J. Carpenter, H. Ade, A. K. Jen, *J. Am. Chem. Soc.* **2015**, *137*, 7616.
- [42] H. Huang, L. Yang, A. Facchetti, T. J. Marks, *Chem. Rev.* **2017**, *117*, 10291.
- [43] N. E. Jackson, B. M. Savoie, K. L. Kohlstedt, M. Olvera de la Cruz, G. C. Schatz, L. X. Chen, M. A. Ratner, *J. Am. Chem. Soc.* **2013**, *135*, 10475.
- [44] T. Lei, X. Xia, J.-Y. Wang, C.-J. Liu, J. Pei, *J. Am. Chem. Soc.* **2014**, *136*, 2135.
- [45] Q. Zhang, L. Yan, X. Jiao, Z. Peng, S. Liu, J. J. Rech, E. Klump, H. Ade, F. So, W. You, *Chem. Mater.* **2017**, *29*, 5990.
- [46] Z.-G. Zhang, Y. Yang, J. Yao, L. Xue, S. Chen, X. Li, W. Morrison, C. Yang, Y. Li, *Angew. Chem., Int. Ed.* **2017**, *56*, 13503.